

## Article

# First-Principles Calculations to Investigate the Effect of Van der Waals Interactions on the Crystal and Electronic Structures of Tin-Based 0D Hybrid Perovskites

Hela Ferjani <sup>1,\*</sup> , Youssef Ben Smida <sup>2</sup>  and Yarub Al-Douri <sup>3,4,5</sup> 

<sup>1</sup> Chemistry Department, College of Science, Imam Mohammad Ibn Saud Islamic University (IMSIU), Riyadh 11623, Saudi Arabia

<sup>2</sup> Laboratory of Valorization of Useful Material, National Centre of Research in Materials Science, University of Carthage, Technopol Borj Cedria, Soliman 8027, Tunisia

<sup>3</sup> Engineering Department, American University of Iraq-Sulaimani, Sulaimani P.O. Box 46001, Kurdistan, Iraq

<sup>4</sup> Department of Mechatronics Engineering, Faculty of Engineering and Natural Sciences, Bahcesehir University, Besiktas, Istanbul 34349, Turkey

<sup>5</sup> Nanotechnology and Catalysis Research Centre, University of Malaya, Kuala Lumpur 50603, Malaysia

\* Correspondence: hhferjani@imamu.edu.sa

**Abstract:** The electronic structures of four tin-based 0D hybrid perovskites ((NH<sub>3</sub>(CH<sub>2</sub>)<sub>2</sub>C<sub>6</sub>H<sub>5</sub>)<sub>2</sub>[SnCl<sub>6</sub>], (C<sub>6</sub>H<sub>10</sub>N<sub>2</sub>)[SnCl<sub>6</sub>], (C<sub>9</sub>H<sub>14</sub>N)<sub>2</sub>[SnCl<sub>6</sub>], and (C<sub>8</sub>H<sub>12</sub>N)<sub>2</sub>[SnCl<sub>6</sub>]) were determined by the DFT method employing the pseudopotential plane wave as implemented in the CASTEP code, and the first transition in each compound has been investigated based on the partial density states and dielectric function. According to the structural properties, incorporating organic cations with the appropriate structure, shape, and strong H-bonding functionality into hybrid perovskite crystals is very beneficial for preventing ion migration and thus enhances the efficiency of hybrid perovskite-based devices. Based on those properties employing the DFT+D method for the dispersion force, the effect of Van der Waals interaction on electronic structure was explained based on the nature of the first electronic transition. The similarity between the experimental and optimized structure was investigated by using a Bilbao crystallographic server. The study of optical properties shows that the Van der Waals interactions have a slight effect on the energy level of the curves. However, the profiles of curves are conserved. The absorption curves of the researched compounds are elaborated.

**Keywords:** perovskite; van der Waals interactions; electronic structure; dielectric function; electronic transition; absorption



**Citation:** Ferjani, H.; Smida, Y.B.; Al-Douri, Y. First-Principles Calculations to Investigate the Effect of Van der Waals Interactions on the Crystal and Electronic Structures of Tin-Based 0D Hybrid Perovskites. *Inorganics* **2022**, *10*, 155. <https://doi.org/10.3390/inorganics10100155>

Academic Editor: Xiangrong Chen

Received: 3 August 2022

Accepted: 21 September 2022

Published: 26 September 2022

**Publisher's Note:** MDPI stays neutral with regard to jurisdictional claims in published maps and institutional affiliations.



**Copyright:** © 2022 by the authors. Licensee MDPI, Basel, Switzerland. This article is an open access article distributed under the terms and conditions of the Creative Commons Attribution (CC BY) license (<https://creativecommons.org/licenses/by/4.0/>).

## 1. Introduction

Organic–inorganic hybrid perovskites have received considerable attention in optoelectronics due to their flexible chemical and structural functionalization. Although photovoltaics is the main focus, their exciting properties inspire applications beyond solar cells, revealing promising utility in light-emitting diodes, lasers, and other optoelectronic devices [1–5]. A significant effort is being put into discovering new perovskite compositions with distinguishable electronic band structures and optical properties.

Lead-based organic–inorganic perovskites show great promise for photovoltaics. This remarkable class of compounds offers a wide range of other fascinating structural possibilities [6–8]. Due to the toxicity of lead, the researchers have focused on appropriate cations for three-dimensional and low-dimensional perovskites such as tin (Sn), bismuth (Bi), antimony (Sb), and indium (In), while maintaining the inherent perovskite properties [8–12]. Furthermore, when compared to lead-based perovskites, these alternative lead-free materials exhibit higher optical absorption coefficients, higher charge carrier mobilities, and a narrower optical band gap [13–15].

However, structure control of organic–inorganic metal halide hybrids has recently been investigated at both the morphological and molecular levels to reduce dimensionality from 3D, 2D, 1D, and 0D. Therefore, the organic cation itself may also play a role in the hybrid materials' special adaptability for photovoltaics (PVs), via a low barrier to readjustment within the structure as well as participation in the dielectric/ferroelectric properties [16–18]. The influence of halide anionic complexes in 0D perovskites has been well studied experimentally and theoretically [19–21]. There are few studies on lead-free 0D perovskites with organic cation replacement.

In the study of Pandech et al. [22] on the effects of Van der Waals interactions on the structural and electronic properties of  $\text{CH}_3\text{NH}_3(\text{Pb}, \text{Sn})(\text{I}, \text{Br}, \text{Cl})_3$  halide perovskites, it was demonstrated that the Van der Waals interactions between the  $\text{MA}^+$  cation and inorganic framework play a critical role in the geometry optimization and electronic properties. Indeed, the implication of Van der Waals interactions gives a better agreement between the optimized and experimental unit cell parameters and allows for a strongly distorted  $\text{BX}_6$  ( $\text{B} = \text{Pb}, \text{Sn}$ ;  $\text{X} = \text{I}, \text{Br}, \text{Cl}$ ) polyhedron that results from  $\text{MA}^+$  cation rotation. These structural transformations affect the electronic structure, which can be changed in the same case from direct to indirect band gap and consequently affect the optical properties.

In other studies of the role of A-cations in the polymorphic stability and optoelectronic properties of lead-free  $\text{ASnI}_3$  perovskites, Ozório et al. [9] demonstrated that the inorganic framework dominates the optical properties, band structure, and density of states around the band edges, which are mainly formed by I p-, Sn s-, and Sn p-states. Consequently, the authors show that the effect of an organic cation can be considered indirect and minimal, affecting mainly the lattice deformations, which do not break the inorganic framework connectivity. They studied the effect of a halide anion ( $\text{X} = \text{Cl}, \text{Br}, \text{I}$ ) and trivalent cation ( $\text{B} = \text{Bi}, \text{Sb}$ ) on the electronic structure and optical properties of hybrid compounds using two organic molecules,  $\text{C}_{20}\text{H}_{20}\text{N}_4\text{B}_{2 \times 10}$  and  $\text{C}_{30}\text{H}_{25}\text{N}_6\text{BX}_6 \cdot 2\text{H}_2\text{O}$  [23]. The authors discovered that the replacement of halide species has a significant impact on the electronic structure and optical properties, and the physical properties change (decrease or increase) almost linearly from  $\text{Cl} \rightarrow \text{Br} \rightarrow \text{I}$ , whereas the effects induced by B are less pronounced. On the other hand, they showed that the valence band is controlled by X p-states, in which the electron binding decreases from  $3\text{p} \rightarrow 4\text{p} \rightarrow 5\text{p}$ , resulting in a decrease in the band energy gap as Cl is replaced by Br and then by I. The role of the organic molecule has a slight effect on the optical gap, as demonstrated in a large series of amine  $[\text{RNH}_3]_2\text{SnI}_4$  hybrid perovskite semiconductors [24,25] where the optical energy gap varies between 1.97 eV and 2.28 eV for about 15 compounds. However, the authors explored a relation between the energy band gap,  $\text{SnI}_3$  polyhedral detorsion, and the Sn-I-Sn band angle.

Previous theoretical studies have focused on determining the HOMO and LUMO energy levels [26–28] that allow to determine the stability of the organic molecules. The experimental determination of the optical band gap has been achieved using a solvent such as water [29], methanol [26], powder [28,30], or thin film [27]. When determining the optical band gap by dissolving the sample in a solvent, periodicity and hydrogen bond interactions are disrupted, which are crucial for determining the electronic structure and optical properties of compounds [19,22,31,32]. In addition, one single optical measurement could be wrong due to an experimental error. Thus, these experimental values should be taken with precaution. Usually, the optical band gap of an interesting material should be determined by several research groups to confirm its optical energy gap value, such as for ZnO [33].

As shown above, there are several works that have studied the effect of the inorganic part of hybrid compounds on the crystallographic and electronic structures and optical properties. On the other side, few studies [19,25,34] have studied the effect of the organic part. In this context, we chose to fix the inorganic part ( $\text{SnCl}_6$ ) and modify the organic molecule to study the effect of the organic molecule on the crystallographic structure, electronic structure, and optical properties. The organic molecules were chosen to be formed by the same elements (C, N, and H). Thus, we are investigating here the effect

of organic molecules on crystallographic and electronic structures and, consequently, on optical properties. The bonding between organic and inorganic components (Van der Waals interaction) is realized by an ordinary ammine group ( $\text{NH}_3$ )<sup>+</sup> that realizes a hydrogen/ionic bond with the halogen atoms. This research could contribute to a greater understanding of the descriptors that influence changes in the structural, energetic, optoelectronic, and excitonic properties of lead-free 0D perovskites. It could also lead to a better understanding of the properties of tin-based 0D hybrid perovskites as a function of organic cation species using a theoretical approach of CASTEP within density functional theory (DFT). The results and discussion are elaborated in Section 2. Section 3 explains the method to achieve this work. Finally, the conclusions are summarized in Section 4.

## 2. Results and Discussion

### 2.1. Structural Properties

Figure 1 depicts the crystal structures of the four 0D perovskite systems ( $(\text{NH}_3(\text{CH}_2)_2\text{C}_6\text{H}_5)_2$ - $[\text{SnCl}_6]$ ,  $(\text{C}_6\text{H}_{10}\text{N}_2)[\text{SnCl}_6]$ ,  $(\text{C}_9\text{H}_{14}\text{N})_2[\text{SnCl}_6]$ , and  $(\text{C}_8\text{H}_{12}\text{N})_2[\text{SnCl}_6]$ ) were used as models for our DFT investigations. The studied compounds crystallize in the monoclinic and triclinic crystal systems (see Table 1). In theory, any single-charged organic cation with enough space within the inorganic crystalline cage could be used to form the perovskite. However, if a cation is extra-large, a perovskite with a low-dimension crystal structure is formed. All crystals in the current work have 0D structures. They displayed the same octahedron morphology as an isolated  $\text{SnCl}_6^{2-}$  octahedron. All of them have octahedra separated by organic molecules: (a), (c), and (d) by one protonated  $(\text{NH}_3(\text{CH}_2)_2\text{C}_6\text{H}_5)^+$ ,  $(\text{C}_9\text{H}_{14}\text{N})^+$ , and  $(\text{C}_8\text{H}_{12}\text{N})^+$  cation, respectively, and (b) by one double protonated  $(\text{C}_6\text{H}_{10}\text{N}_2)^{2+}$  cation. It has been described that the strong hydrogen bonding exists between organic cations and inorganic framework halogen atoms, which influences octahedral distortion [35–37].

**Table 1.** Summary of the Van der Waals interactions in the different structures.

Compound	Compound Name	Crystal System/ Space Group	Number of Donor Atoms	N-H...Cl Hydrogen Bonds	$\pi$ - $\pi$ Interactions	$E_g^{\text{exp}}$ (eV)	Ref
a	$(\text{NH}_3(\text{CH}_2)_2\text{C}_6\text{H}_5)_2\text{SnCl}_6$	Monoclinic $P2_1/c$	1 Nitrogen atoms $\text{NH}_3^+$	4 Strong	4 Weak	-	[1]
b	$(\text{C}_6\text{H}_{10}\text{N}_2)\text{SnCl}_6$	Monoclinic $P2_1/c$	2 Nitrogen atoms $\text{NH}^+/\text{NH}_3^+$	5 Strong	2 Weak	3.56 Thin film	[2]
c	$(\text{C}_9\text{H}_{14}\text{N})_2$ $\text{SnCl}_6$	Monoclinic $C2/m$	1 Nitrogen atom $\text{NH}_3^+$	4 Strong	1 Weak	5.2 Solid	[3]
d	$(\text{C}_8\text{H}_{12}\text{N})_2\text{SnCl}_6$	Triclinic $P-1$	1 Nitrogen atom $\text{NH}_3^+$	5 Strong	2 Weak	4.11 In water	[4]

We compared the four free organic cations in terms of their H-bond donating abilities, considering their shape, polarity, and spatial–structural orientation, as a first step in analyzing the H-bonding interactions between organic cations and inorganic framework, as well as their impact on the energy band gap [35]. These characteristics of organic cations affect their ability to integrate into the perovskite framework as well as their bonding strength with chlorine atoms. We discovered that all four organic cations are  $\pi$ -conjugated systems with (a), (c), and (d) structures having organic cations with one donor atom (three polar N-H bonds at the  $\text{NH}_3^+$  terminus), and (b) having two donor atoms (one spatially separated pair of more polar N-H bond and one polar N-H bonds at the  $\text{NH}^+$  terminus) (see Table 1). As a result, structural cohesion is higher for (b) than for (a), (c), and (d). Table 1 presents that the number and nature (weak or strong) of hydrogen bonds and  $\pi$ - $\pi$  interactions are independent of the number of donor atoms but depend on the crystalline structure. In all structures,  $\pi$ -stacked interactions are observed between the organic molecules (see Table 1). In these systems, the formation of  $\pi$ -stacks is important because it can introduce a pathway for charge transport through the organic layers. Furthermore, the hydrogen bonding and

$\pi$ -stacking interactions appear to be an important factor in crystal packing stability. On the other hand, the optical energy gap values of the studied compounds are indicated in Table 1, but usually, it is difficult to confirm the certitude of an experimental value for only a one-time measurement.

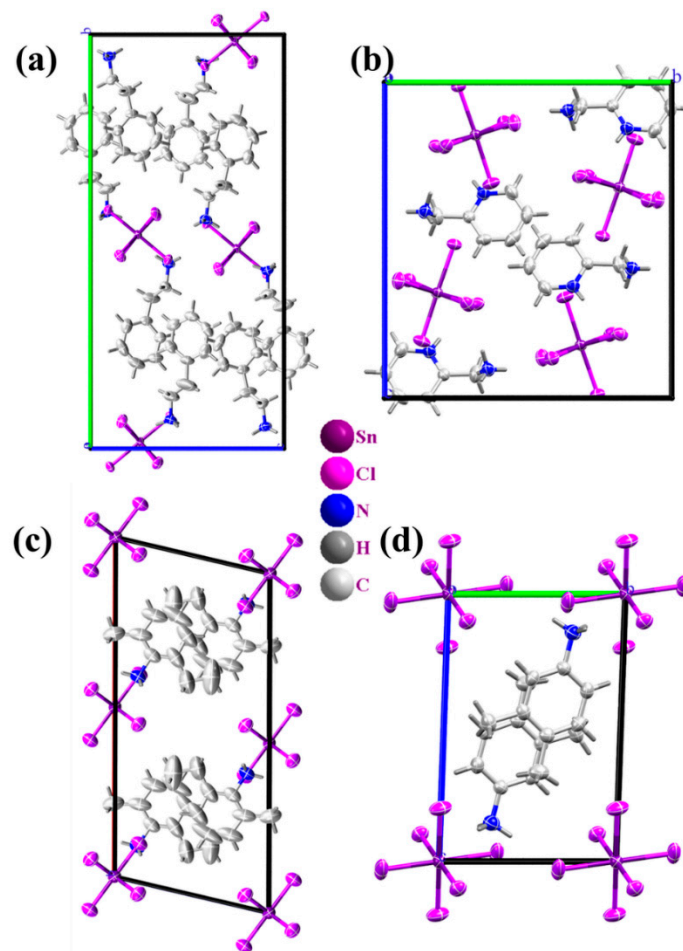


**Figure 1.** Projection of crystal structure of the four perovskites (a)  $(\text{NH}_3(\text{CH}_2)_2\text{C}_6\text{H}_5)_2[\text{SnCl}_6]$ , (b)  $(\text{C}_6\text{H}_{10}\text{N}_2)[\text{SnCl}_6]$ , (c)  $(\text{C}_9\text{H}_{14}\text{N})_2[\text{SnCl}_6]$ , and (d)  $(\text{C}_8\text{H}_{12}\text{N})_2[\text{SnCl}_6]$ , which were employed to model the perovskites in this work using substitution of organic cations.

The octahedral distortion can be defined by the quantity [38]:

$$\Delta = 1/6 \sum [(R_i - \bar{R})/\bar{R}]^2 \quad (1)$$

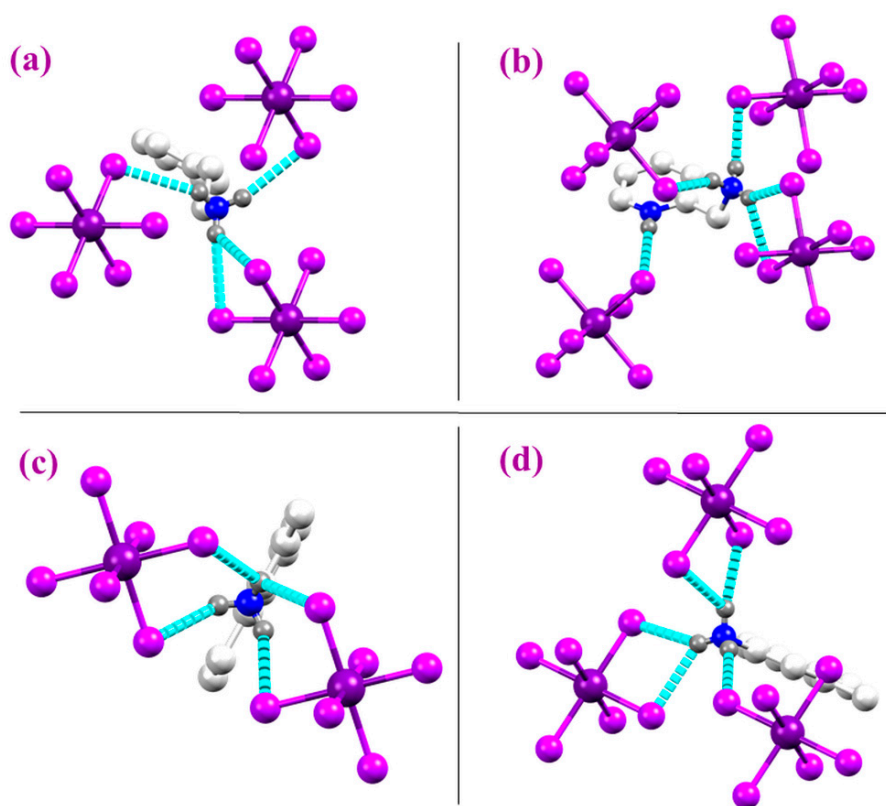
where  $\bar{R}$  is average bond length and  $R_i$  is an individual bond length.

Table 2 displays the  $\Delta$ -values for all perovskite structure types investigated in this work. All average bond lengths  $\bar{R}$  have rather similar values. The  $\text{SnCl}_6^{2-}$  ion is octahedrally imposed by an  $\text{AX}_6$  electron configuration of the central atom's valence shell. Despite having a maximum distortion of  $5.5 \times 10^{-5}$  in compound (b), the  $\text{SnCl}_6^{2-}$  anion in (b) should still be considered a regular octahedron. Multiple hydrogen bonds influence the interlayer distance at the same time, greatly shortening the  $\text{Cl} \cdots \text{Cl}$  distance (see Table 2). Because of the larger size and stereochemical configuration of organic cations in (a), (c), and (d), the inorganic layers have a larger dispersion, with values of 13.326, 10.517, and 10.684, respectively. Due to the strength and multiple hydrogen bonds, they can attract the inorganic layers to become closer, and the distance between the inorganic layers is greatly reduced to 3.456 and 6.858 for (b) and (d), respectively.

**Table 2.** Structure perovskite types with  $\Delta$ -values as a measure for distortion of the  $\text{SnCl}_6$  octahedron.

Compound	Space Group	$\bar{R}$ (Å)	$\Delta$ ( $10^{-5}$ )	Inorganic Interlayer Distance (Å)	$d\text{Cl} \cdots \text{Cl}$ (Å)
a	$P2_1/c$	2.423994	1	13.326	9.760
b	$P2_1/c$	2.422345	5.5	7.668	3.456
c	$C2/m$	2.424254	1.4	10.517	7.175
d	$P-1$	2.427381	5.4	10.684	6.858

Figure 2 illustrates the formation of hydrogen-bonding networks between the hydrogen of amino groups in organic cations and terminal chlorine ions in the  $\text{SnCl}_6^{2-}$  framework, which is highlighted by a cyan dashed line. Binding with terminal chloride ions is responsible to some extent for the slight distortion.



**Figure 2.** N-H  $\cdots$  Cl hydrogen bond interactions in: (a)  $(\text{NH}_3(\text{CH}_2)_2\text{C}_6\text{H}_5)_2[\text{SnCl}_6]$ , (b)  $(\text{C}_6\text{H}_{10}\text{N}_2)[\text{SnCl}_6]$ , (c)  $(\text{C}_9\text{H}_{14}\text{N})_2[\text{SnCl}_6]$ , and (d)  $(\text{C}_8\text{H}_{12}\text{N})_2[\text{SnCl}_6]$ .

## 2.2. Electronic Structure

Based on the theoretical study of  $[\text{RNH}_3]_2\text{SnI}_4$  [24,25] (R = ramification),  $\text{C}_{20}\text{H}_{20}\text{N}_4\text{B}_2\text{X}_{10}$  and  $\text{C}_{30}\text{H}_{25}\text{N}_6\text{BX}_6 \cdot 2\text{H}_2\text{O}$  [23] (X = Cl, Br, I; B = Bi, Sb) hybrid perovskite semiconductors, it can be noticed that the optical energy gap depends basically on the inorganic part. However, the organic molecule has a slight effect. On the other hand, the energy gap depends on the distortion of the inorganic polyhedral. This distortion could be a result of the Van der Waals interactions between the organic molecule and inorganic polyhedron. Therefore, the Van der Waals interaction must be considered in the calculation to show a good agreement between the experimental and optimized unit cell parameters [9].

Thus, in this part, we explain and discuss the electronic structure of the studied compounds using the GGA-PBE scheme without considering Van der Waals interaction. Since the different materials are formed by the same chemical elements (C, N, H, Sn, and Cl), then the variations in band energy gap and optical properties are due to crystal

structures [39], organic cation formula [40–42], and maybe octahedral distortion. In the next part, we see the effect of Van der Waals interaction on crystal structure and electronic structure, and in the fourth part, the absorption of different compounds is discussed.

The GGA-PBE method is used since in the previous works [43–45]. We found the calculated values of optical energy gap very close to the experimental values. On the other hand, another study finds that the energy gap value is underestimated [46–48] when compared to the experimental value. This underestimation may be corrected by considering Van der Waals interaction.

The calculated electronic band structures using the GGA-PBE method of the four tin hybrid organic–inorganic materials ( $(\text{NH}_3(\text{CH}_2)_2\text{C}_6\text{H}_5)_2[\text{SnCl}_6]$ ,  $(\text{C}_6\text{H}_{10}\text{N}_2)[\text{SnCl}_6]$ ,  $(\text{C}_9\text{H}_{14}\text{N})_2[\text{SnCl}_6]$ , and  $(\text{C}_8\text{H}_{12}\text{N})_2[\text{SnCl}_6]$ ) are shown in Figure 3. The studied materials are labeled with letters a, b, c, and d for  $(\text{NH}_3(\text{CH}_2)_2\text{C}_6\text{H}_5)_2[\text{SnCl}_6]$ ,  $(\text{C}_6\text{H}_{10}\text{N}_2)[\text{SnCl}_6]$ ,  $(\text{C}_9\text{H}_{14}\text{N})_2[\text{SnCl}_6]$ , and  $(\text{C}_8\text{H}_{12}\text{N})_2[\text{SnCl}_6]$ , respectively (Tables 1 and 2). The analysis of Figure 3 shows that the compounds (a) and (d) are direct band gap semiconductors. However, the compounds b and c are indirect band gap semiconductors. The estimated energy gap values vary between 3.044 eV and 3.152 eV (see Table 2). The variation in the optical energy gap between the different structures is small (maximum of 0.11 eV). This small variation is due to the fact that all the compounds have the same inorganic compound.

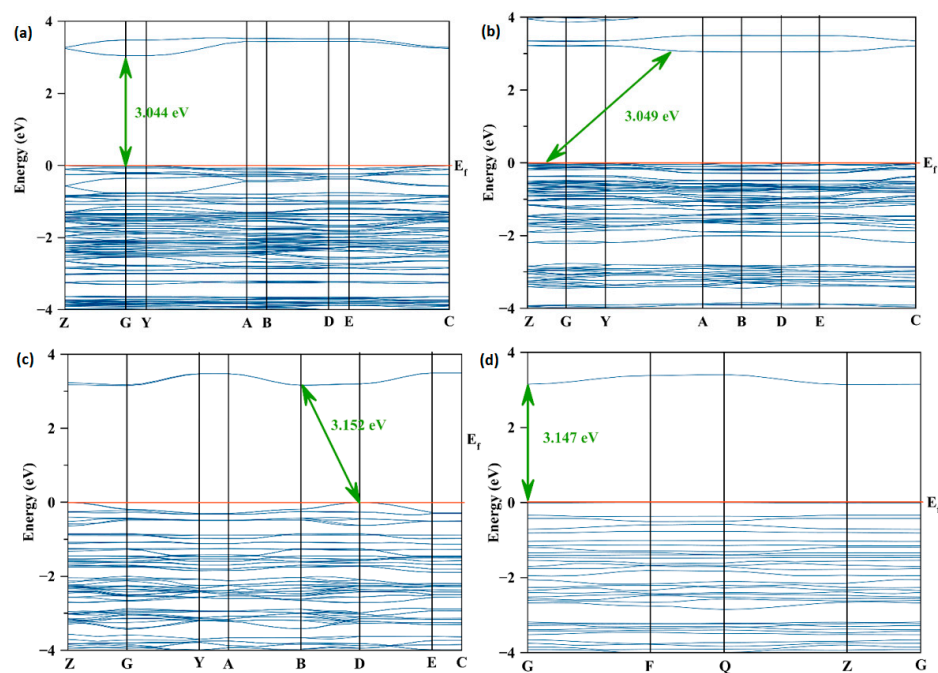


**Figure 3.** Electronic band structure of four tin (IV)-based hybrids: (a)  $(\text{NH}_3(\text{CH}_2)_2\text{C}_6\text{H}_5)_2[\text{SnCl}_6]$ , (b)  $(\text{C}_6\text{H}_{10}\text{N}_2)[\text{SnCl}_6]$ , (c)  $(\text{C}_9\text{H}_{14}\text{N})_2[\text{SnCl}_6]$ , and (d)  $(\text{C}_8\text{H}_{12}\text{N})_2[\text{SnCl}_6]$ .

To more understand the electronic structure of different tin organic–inorganic hybrids, the total density of states (TDOS) and the partial density of states (PDOS) of different elements are calculated, as presented in Figure 4. The total density of states of different compounds (Figure 4) illustrates that the four compounds have the deepest states at about  $-20$  eV, which means that the studied compounds are in the same order of stability.

Figure 4 shows the deeper sub-band valence in the four compounds ( $(\text{NH}_3(\text{CH}_2)_2\text{C}_6\text{H}_5)_2[\text{SnCl}_6]$ ,  $(\text{C}_6\text{H}_{10}\text{N}_2)[\text{SnCl}_6]$ ,  $(\text{C}_9\text{H}_{14}\text{N})_2[\text{SnCl}_6]$ , and  $(\text{C}_8\text{H}_{12}\text{N})_2[\text{SnCl}_6]$ ) is formed mainly by s-states of carbon and nitrogen atoms. For all structures, the upper valence sub-band is formed mainly by p-states of carbon and s-states of hydrogen atoms, except for compound (b), where the upper valence sub-band is formed mainly by p-states of chlorine and s-states of hydrogen atoms. On the other hand, the conduction band consists of s-states of Sn and p-states of Cl and a small contribution of p-states of carbon atoms for the structure (b).

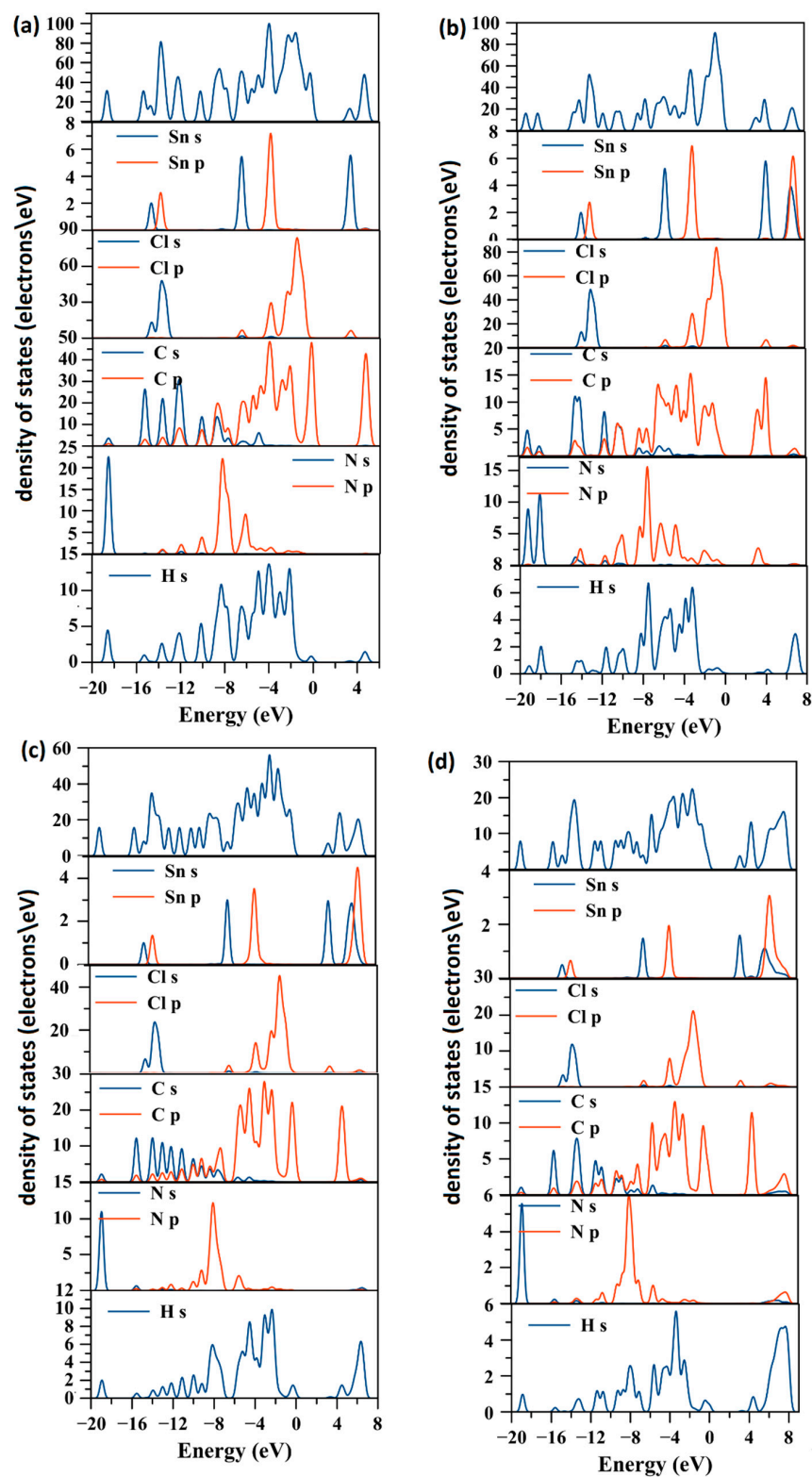


**Figure 4.** Total and partial density of states of different studied tin (IV) hybrid organic–inorganic materials: (a)  $(\text{NH}_3(\text{CH}_2)_2\text{C}_6\text{H}_5)_2[\text{SnCl}_6]$ , (b)  $(\text{C}_6\text{H}_{10}\text{N}_2)[\text{SnCl}_6]$ , (c)  $(\text{C}_9\text{H}_{14}\text{N})_2[\text{SnCl}_6]$ , and (d)  $(\text{C}_8\text{H}_{12}\text{N})_2[\text{SnCl}_6]$ .

It can be noticed that the s- and p-states of tin and chlorine have the same profile in the four structures with a slight modification. However, the other states forming the electronic structures are different. Thus, we can conclude that the electronic structure depends on the

organic molecule. In addition, the intensity of s- and p-states of tin and chlorine depends on the number of octahedra in the unit cell. The same remark can be made for the other states forming the compounds.

### 2.3. Dielectric Function and Determination of the First Transition

To understand the effect of Van der Waals interaction on the electronic structure, we determine the nature of first transition from band valence by using the imaginary part of the dielectric function and partial density of states.

The dielectric function  $\varepsilon(\omega)$  [49] describes the interaction between electromagnetic waves and electrons in matter. It connects the electronic structure of a material to the physical process of transition. The dielectric function can be written as [50]:

$$\varepsilon(\omega) = \varepsilon_1(\omega) + i\varepsilon_2(\omega) \quad (2)$$

where  $\varepsilon_1(\omega)$  and  $\varepsilon_2(\omega)$  denote the real (dispersive) and the imaginary (absorptive) parts, respectively [51], and  $\varepsilon_2(\omega)$  can be calculated from direct numerical evaluations of momentum matrix elements of the electric dipole operator between the conduction and valence band wave functions [52]:

$$\varepsilon_2(\omega) = \left(\frac{2e^2\pi}{\omega\varepsilon_0}\right) \sum_{kvc} |\langle \psi_k^c | u \cdot r | \psi_k^v \rangle|^2 \delta(E_k^c - E_k^v - E) \quad (3)$$

where  $\psi_k^c$  and  $\psi_k^v$  are the conduction and valence band wave functions at  $k$ , respectively,  $u$  is the polarization vector of the incident electric field,  $r$  is the electron's radius vector,  $\varepsilon_0$  is vacuum permittivity, and  $e$  is electric charge.

The real part  $\varepsilon_1(\omega)$  can be obtained from the imaginary part by using the Kramers–Krönig dispersion equation [52,53]:

$$\varepsilon_1(\omega) = 1 + \frac{2}{\pi} p \int_0^\infty \frac{\omega' \varepsilon_2(\omega') d\omega'}{\omega'^2 - \omega^2} \quad (4)$$

where  $p$  is the principal value of the integral.

The unpolarized variation in real and imaginary parts of the dielectric function as a function of energy is regrouped in Figure 5. From the  $\varepsilon_1$  curve, it is possible to determine the static dielectric function  $\varepsilon_1(0)$ , which is approximately 2 for (a), (b), and (c) and about 2.5 for the compound (d). On the other hand, it is remarkable that the  $\varepsilon_1$  curves of the structures (a) and (b) have negative values at about 6 eV and 8 eV, respectively, which correspond to a metallic behavior [54].

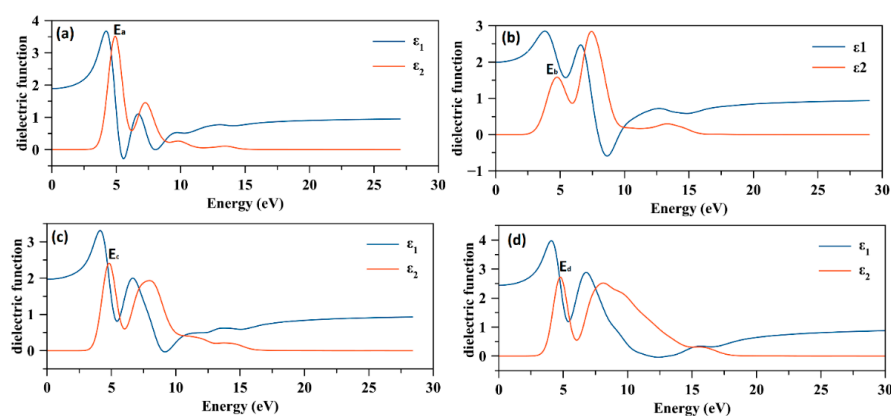


**Figure 5.** Variation in the real and imaginary parts of the dielectric function as function of energy of the different studied compounds: (a)  $(\text{NH}_3(\text{CH}_2)_2\text{C}_6\text{H}_5)_2[\text{SnCl}_6]$ , (b)  $(\text{C}_6\text{H}_{10}\text{N}_2)[\text{SnCl}_6]$ , (c)  $(\text{C}_9\text{H}_{14}\text{N})_2[\text{SnCl}_6]$ , and (d)  $(\text{C}_8\text{H}_{12}\text{N})_2[\text{SnCl}_6]$ .

From  $\varepsilon_2$  curves it is possible to deduce the same information about the electronic transition in the studied materials. Figure 5 shows that the four compounds ( $(\text{NH}_3(\text{CH}_2)_2\text{C}_6\text{H}_5)_2[\text{SnCl}_6]$ ,  $(\text{C}_6\text{H}_{10}\text{N}_2)[\text{SnCl}_6]$ ,  $(\text{C}_9\text{H}_{14}\text{N})_2[\text{SnCl}_6]$  and  $(\text{C}_8\text{H}_{12}\text{N})_2[\text{SnCl}_6]$ ) each have at least four electronic transitions, and the first one corresponds to the lowest transition energy, where the energy corresponds to the optical energy gap. The intensity of first transition is about 2.5 for the structures (b), (c), and (d) and about 3.5 for the structure (a). The first transitions are labeled by the letters  $E_a$ ,  $E_b$ ,  $E_c$ , and  $E_d$  in the  $\varepsilon_2$  curves.

The first transition is the transition with the lowest energy from the valence band to conduction band. The TDOS and PDOS allow us to identify the different states that could participate in the first transition. Then, by using the selection rule ( $\Delta l = 0, \mp 1$  (no  $0 \rightarrow 0$  transition) [55,56] and based on structural study and dielectric function, it is possible to determine the nature of the first transition responsible for the energy band gap for each compound.

The four structures ( $(\text{NH}_3(\text{CH}_2)_2\text{C}_6\text{H}_5)_2[\text{SnCl}_6]$ ,  $(\text{C}_6\text{H}_{10}\text{N}_2)[\text{SnCl}_6]$ ,  $(\text{C}_9\text{H}_{14}\text{N})_2[\text{SnCl}_6]$  and  $(\text{C}_8\text{H}_{12}\text{N})_2[\text{SnCl}_6]$ ) each have the following orbital:  $\text{H}|s\rangle$ ,  $\text{Cl}|s\rangle$ ,  $\text{Cl}|p\rangle$ ,  $\text{Cl}|s\rangle$ ,  $\text{Cl}|p\rangle$ ,  $\text{Sn}|s\rangle$ ,  $\text{N}|s\rangle$ , and  $\text{N}|p\rangle$ . Based on the selection rule and partial density of states, we can find six possible transitions in the studied materials:  $\text{H}|s\rangle \rightleftharpoons \text{Cl}|p\rangle$ ;  $\text{H}|s\rangle \rightleftharpoons \text{Cl}|p\rangle$ ;  $\text{H}|s\rangle \rightleftharpoons \text{N}|p\rangle$ ;  $\text{Sn}|s\rangle \rightleftharpoons \text{Cl}|p\rangle$ ;  $\text{Sn}|s\rangle \rightleftharpoons \text{Cl}|p\rangle$ ;  $\text{Sn}|s\rangle \rightleftharpoons \text{N}|p\rangle$ . To determine which one is the first transition, we determined the position of maximum of each partial state in the conduction band  $E_c$  and valence band  $E_v$ . Table 3 summarizes the position of partial states on the energy axis [54]. Table 4 presents the possible first transition and energy corresponding thereto, deduced from the dielectric function and the partial density of states. The energy of the first transition was determined directly from the curves (Figure 5). For the  $\Delta E_{v \rightarrow c}$ , all possible combinations were calculated and only those which have energy close the  $E_{\varepsilon_2}$  were conserved (Table 4).

**Table 3.** Position of the partial states on the energy axis for the different studied compounds.

Energy States		$E_v$				$E_c$				
		$\text{Cl} p\rangle$	$\text{Cl} p\rangle$	$\text{N} p\rangle$	$\text{H} s\rangle$	$\text{H} s\rangle$	$\text{Sn} s\rangle$	$\text{Cl} p\rangle$	$\text{Cl} p\rangle$	$\text{N} p\rangle$
Compound	a	-1.45	-0.20	-1.52	-0.18	4.71	3.43	3.43	4.72	—
	b	-0.67	-1.08	-0.73	-0.80	3.34	4.18	4.18	3.31	3.31
	c	-1.50	-0.35	-0.47	-0.31	3.34	3.37	3.38	4.50	6.36
	d	-1.51	-0.50	-1.58	-0.45	3.27	3.27	3.28	4.41	7.70

**Table 4.** The possible first transition and the energy corresponding deduced from the dielectric function and the partial density of states.

Label	$E_{\varepsilon_2}$ (1st Transition)	Transition	$\Delta E_{v \rightarrow c} = E_c - E_v$
$E_a$	4.91	$\text{H} s\rangle \rightleftharpoons \text{Cl} p\rangle$	4.91
		$\text{Sn} s\rangle \rightleftharpoons \text{Cl} p\rangle$	4.88
$E_b$	4.79	$\text{Sn} s\rangle \rightleftharpoons \text{Cl} p\rangle$	4.85
$E_c$	4.80	$\text{Sn} s\rangle \rightleftharpoons \text{Cl} p\rangle$	4.87
		$\text{H} s\rangle \rightleftharpoons \text{Cl} p\rangle$	4.84
$E_d$	4.78	$\text{Sn} s\rangle \rightleftharpoons \text{Cl} p\rangle$	4.78
		$\text{H} s\rangle \rightleftharpoons \text{Cl} p\rangle$	4.78

Table 4 displays that the four compounds ( $(\text{NH}_3(\text{CH}_2)_2\text{C}_6\text{H}_5)_2[\text{SnCl}_6]$ ,  $(\text{C}_6\text{H}_{10}\text{N}_2)[\text{SnCl}_6]$ ,  $(\text{C}_9\text{H}_{14}\text{N})_2[\text{SnCl}_6]$  and  $(\text{C}_8\text{H}_{12}\text{N})_2[\text{SnCl}_6]$ ) share the possibility of transition  $\text{Sn}|s\rangle \rightleftharpoons \text{Cl}|p\rangle$ , which corresponds to an electronic transition in an inorganic octahedron. In addition, the structures (c) and (d) have another transition  $\text{H}|s\rangle \rightleftharpoons \text{Cl}|p\rangle$ . However, the structure a has the second transition as:  $\text{H}|s\rangle \rightleftharpoons \text{Cl}|p\rangle$ . From these results, it is possible to deduce that the compounds (a), (c), and (d) are sensible to the Van der Waals interaction more than the compound (b). In addition, the structures (c) and (d) have the same behavior versus the

hydrogen interaction. These results may be useful to investigate the effect of the Van der Waals interaction on the electronic structures of the studied compounds.

#### 2.4. Effect of the Van der Waals Interactions on the Crystallographic and Electronic Structures

The structural study shows the presence of Van der Waals interactions (see Table 1). Thus, DFT+D calculations were performed to quantify the effect of these types of interactions on the structures and optical energy gap values. For the first time since the modification of the unit cell affected the optical energy gap values, the structures were optimized with constant unit cell parameters using the DFT and DFT+D methods, the methods that show a consistent modification of the optical energy gap that was used a second time with the optimization of a unit cell. The optimized structures were compared to experimental structures using a Bilbao crystallographic server [52,57]. Table 3 summarizes the optical energy gap values using different methods to study the effect of Van der Waals interaction utilizing CASTEP code.

Table 5 displays that the effect of Van der Waals interaction is significant for the structure (a) using the GGA-PW91+OBS scheme in comparison with the others and has a slight effect for the structures (c) and (d). In addition, the structure (b) is not affected by the implication of Van der Waals interactions. The GGA-PBE+TS and GGA-PBE-Grimme have the same effect on optical energy gap for the structures (c) and (d) where the optical energy gap has been decreased. Based on these results, the unit cells of four structures were optimized using the correction, showing a difference when Van der Waals interactions are implied. Table 6 depicts the unit cell and optical energy gap values.

**Table 5.** Calculated optical gap energies of the different studied compound using DFT and DFT+D.

Methods	a	b	c	d
GGA-PBE	3.042	3.049	3.152	3.147
GGA-PBE+TS	2.988	3.056	3.063	3.072
GGA-PBE-Grimme	2.985	3.058	3.078	3.092
GGA-PW91	3.081	3.057	3.158	3.167
GGA-PW91+OBS	3.341	3.057	3.172	3.151

**Table 6.** Experimental and optimized unit cell parameters and calculated optical gap energies with different studied structures using DFT and DFT+D methods.

Compound	Scheme	a (Å)	b (Å)	c (Å)	$\alpha$ (°)	$\beta$ (°)	$\gamma$ (°)	V (Å <sup>3</sup> )	E <sub>g</sub> (eV)
a	Exp	7.345	25.667	11.971	-	90.106	-	2256.8	-
	GGA-PW91	7.4315	25.8404	12.1654	-	90.1286	-	2336.15	3.115
	GGA-PW91+OBS	7.2527	25.5844	11.8856	-	90.2596	-	2205.42	3.043
b	Exp	7.0566	13.5254	14.8999	-	94.703	-	1417.31	-
	GGA-PBE	7.1286	13.6778	15.0881	-	94.4060	-	1466.80	2.971
	GGA-PBE+TS	7.0537	13.5895	14.9690	-	94.5887	-	1430.27	3.026
c	Exp	19.7521	7.2293	9.2181	-	103.046	-	1282.31	-
	GGA-PBE	19.8713	7.3406	9.3495	-	103.363	-	1326.86	3.216
	GGA-PBE+TS	19.7328	7.1942	9.3148	-	103.4064	-	1286.31	3.084
d	Exp	7.4904	7.9864	10.6842	91.572	90.470	117.5410	566.34	-
	GGA-PBE	7.6320	8.0769	10.7584	91.4226	90.5358	117.9866	585.28	3.227
	GGA-PBE+TS	7.5157	7.9947	10.6920	91.5932	90.4239	117.6723	568.58	3.077

By using the Bilbao crystallographic server [52,57], the structure similarity was evaluated. Indeed, four parameters were calculated: the degree of lattice distortion  $s$ ; the maximum displacement between the atomic positions of paired atoms  $d_{\max}$ ; arithmetic mean of the distance  $d_{\text{av}}$ ; and similarity function  $\Delta$  [58]. The values of these calculated parameters for the four structures ((NH<sub>3</sub>(CH<sub>2</sub>)<sub>2</sub>C<sub>6</sub>H<sub>5</sub>)<sub>2</sub>[SnCl<sub>6</sub>], (C<sub>6</sub>H<sub>10</sub>N<sub>2</sub>)[SnCl<sub>6</sub>], (C<sub>9</sub>H<sub>14</sub>N)<sub>2</sub>[SnCl<sub>6</sub>] and (C<sub>8</sub>H<sub>12</sub>N)<sub>2</sub>[SnCl<sub>6</sub>]) by using two optimization schemes are listed in Table 7.

**Table 7.** Evaluation of the structure's similarity.

Structure	XC	S	$d_{\max}$ (Å)	$d_{\text{av}}$ (Å)	$\Delta$
a (NH <sub>3</sub> (CH <sub>2</sub> ) <sub>2</sub> C <sub>6</sub> H <sub>5</sub> ) <sub>2</sub> [SnCl <sub>6</sub> ]	GGA-PW91	0.0069	0.5130	0.1939	0.027
	GGA-PW91+OBS	0.0051	0.5240	0.2065	0.043
b (C <sub>6</sub> H <sub>10</sub> N <sub>2</sub> )[SnCl <sub>6</sub> ]	GGA-PBE	0.0067	0.2736	0.0961	0.015
	GGA-PBE+TS	0.0023	0.2854	0.0993	0.022
c (C <sub>9</sub> H <sub>14</sub> N) <sub>2</sub> [SnCl <sub>6</sub> ]	GGA-PBE	0.0071	0.3841	0.1425	0.035
	GGA-PBE+TS	0.0040	0.3909	0.1486	0.026
d (C <sub>8</sub> H <sub>12</sub> N) <sub>2</sub> [SnCl <sub>6</sub> ]	GGA-PBE	0.0070	0.1707	0.0824	0.035
	GGA-PBE+TS	0.0012	0.1873	0.0870	0.022

In the comparison between the experimental and optimized unit cells in Table 6, it can be seen that the implication of the dispersive interaction allows to obtain unit cell parameters very close to the experimental value. In addition, for the structure (c) the optimization of the unit cell allows to increase the optical energy gap. However, the implication of the Van der Waals interaction decreases the value of the optical energy.

Figure 6 shows the electronic band structure of (a) (NH<sub>3</sub>(CH<sub>2</sub>)<sub>2</sub>C<sub>6</sub>H<sub>5</sub>)<sub>2</sub>[SnCl<sub>6</sub>]; (b) (C<sub>6</sub>H<sub>10</sub>N<sub>2</sub>)[SnCl<sub>6</sub>]; (c) (C<sub>9</sub>H<sub>14</sub>N)<sub>2</sub>[SnCl<sub>6</sub>], and (d) (C<sub>8</sub>H<sub>12</sub>N)<sub>2</sub>[SnCl<sub>6</sub>], without dispersion interaction with index 1, and with the dispersion interaction index 2. The scheme and the approximation for each structure are indicated in the figure. The first observation is that the different materials conserve the nature of the gap (direct or indirect). Thus, the modifications seen in Figure 6 are in relation only of the value of the optical gap.

Obviously, the optical energy gap is affected by the implication of dispersive interaction. The Van der Waals interaction, with the exception of structure (c), allows for a decrease in the optical energy gap value. This structure is not affected by the dispersive interactions when the unit cell parameters are not optimized, thus this variation may be due to unit cell parameter variation.

To explain these variations, we discuss the effect of Van der Waals interaction on the first transition on each material. First, for structure (b), only one transition was determined, which is Sn |s>  $\rightleftharpoons$  Cl |p>, which means the optical energy gap does not depend on Van der Waals interactions and slight variation is detected due to variation in unit cell parameters.

For the structures (c) and (d), two transitions were seen: Sn |s>  $\rightleftharpoons$  Cl |p> and H |s>  $\rightleftharpoons$  Cl |p>. Thus, they depend on Van der Waals interaction. Therefore, the optical energy gaps are decreased.

For the structure (a), it had the transition Sn |s>  $\rightleftharpoons$  Cl |p> in octahedron and a second possible transition H |s>  $\rightleftharpoons$  Cl |p>, which is different from the transition seen for the compounds (c) and (d). Thus, the effect of Van der Waals interaction is not the same.

In the structures (a), (c), and (d), the introduction of Van der Waals interaction in the calculation allows to consider that hydrogen bond is an attractive force which allows to decrease the optical energy gap.

Table 7 displays the evaluation of the similarity between the experimental and optimized structure. These results show that the use of dispersive interactions allows to have an optimized structure very similar to the experimental one, and this can be verified by comparing the values of parameters of similarity. On the other hand, the use or not of Van der Waals interactions gives close values of maximum and average displacements.

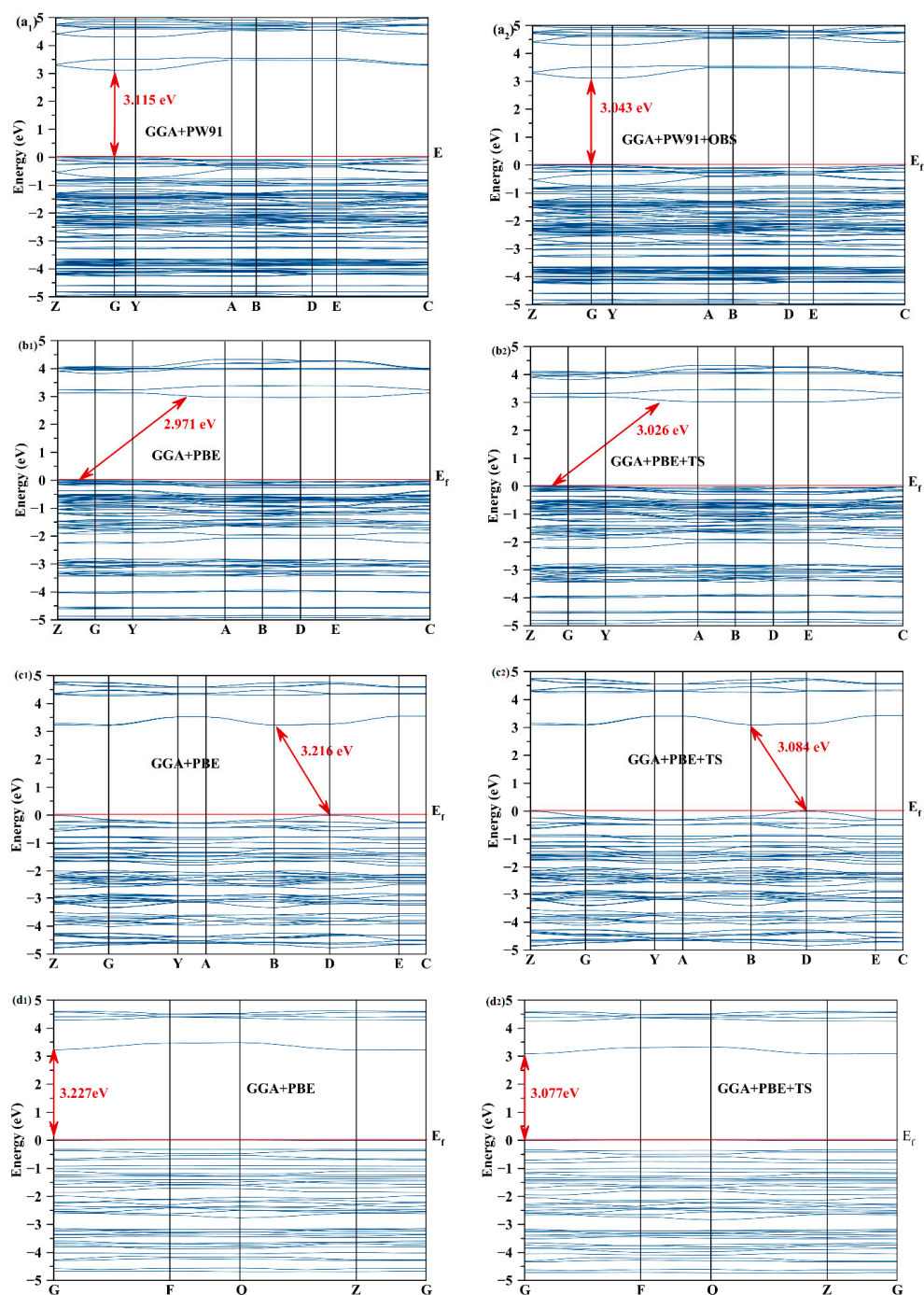


**Figure 6.** Electronic band structure (a1,a2)  $(\text{NH}_3(\text{CH}_2)_2\text{C}_6\text{H}_5)_2[\text{SnCl}_6]$ , (b1,b2)  $(\text{C}_6\text{H}_{10}\text{N}_2)[\text{SnCl}_6]$ , (c1,c2)  $(\text{C}_9\text{H}_{14}\text{N})_2[\text{SnCl}_6]$ , and (d1,d2)  $(\text{C}_8\text{H}_{12}\text{N})_2[\text{SnCl}_6]$ , without dispersion interaction with index 1, and with the dispersion interaction index 2. The scheme and the approximation for each structure are indicated on the figure.

### 2.5. Absorption

The absorption coefficient  $\alpha(\omega)$  is an important optical property of a material. It can be calculated from the dielectric function, as the following equation:

$$\alpha(\omega) = \sqrt{2} \left[ \sqrt{\varepsilon_1^2(\omega) + \varepsilon_2^2(\omega)} - \varepsilon_1(\omega) \right]^{1/2} \quad (5)$$

The variation in the absorption  $\alpha(\omega)$  of the four compounds  $\text{NH}_3(\text{CH}_2)_2\text{C}_6\text{H}_5)_2[\text{SnCl}_6]$ ,  $(\text{C}_6\text{H}_{10}\text{N}_2)[\text{SnCl}_6]$ ,  $(\text{C}_9\text{H}_{14}\text{N})_2[\text{SnCl}_6]$ , and  $(\text{C}_8\text{H}_{12}\text{N})_2[\text{SnCl}_6]$  as a function of energy is represented in Figure 7.

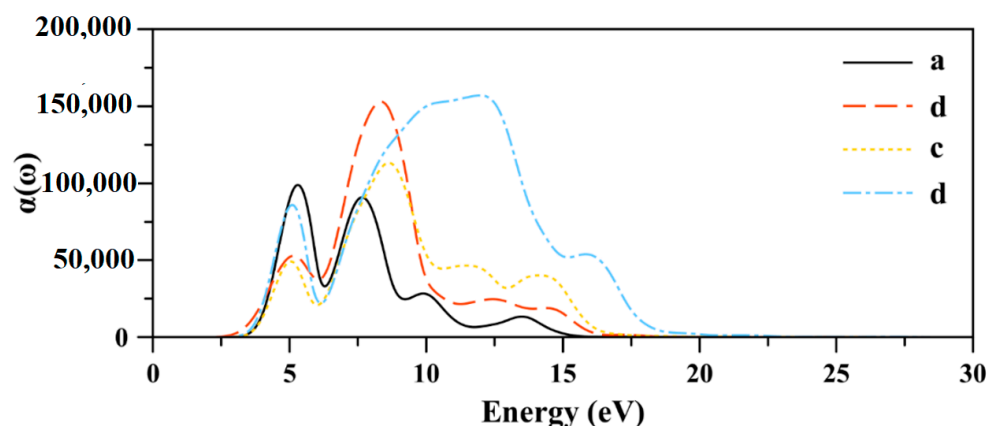


**Figure 7.** Variation in absorption as function of energy of (a)  $(\text{NH}_3(\text{CH}_2)_2\text{C}_6\text{H}_5)_2[\text{SnCl}_6]$ , (b)  $(\text{C}_6\text{H}_{10}\text{N}_2)[\text{SnCl}_6]$ , (c)  $(\text{C}_9\text{H}_{14}\text{N})_2[\text{SnCl}_6]$ , and (d)  $(\text{C}_8\text{H}_{12}\text{N})_2[\text{SnCl}_6]$ .

The implication that the Van der Waals interaction is using different methods of optimization does not modify the profile of absorption curves, and they slightly change the intensity. In this part, we discuss qualitatively the variation in absorption of the studied compounds as a function of energy.

Figure 7 shows that the four compounds are absorbers between 3 and 20 eV with a maximum absorption in the UV region and slightly in the visible region. The studied compounds have four band absorptions for each. The maximum absorption is about  $98 \times 10^3 \text{ cm}^{-1}$  at 5.30 eV for the structure (a) and about  $15 \times 10^4 \text{ cm}^{-1}$  for the structures (b) and (d) at 8.17 eV and 12.04 eV, respectively. For the structure (c), the maximum absorption is about  $11 \times 10^4$  at 8.71 eV.

### 3. Computational Methods

First-principles calculations were carried out based on the density functional theory (DFT) method by employing the pseudopotential plane wave as implemented in the CASTEP code [58,59]. The experimental structural models of the four compounds  $\text{NH}_3(\text{CH}_2)_2\text{C}_6\text{H}_5)_2[\text{SnCl}_6]$ ,  $(\text{C}_6\text{H}_{10}\text{N}_2)[\text{SnCl}_6]$ ,  $(\text{C}_9\text{H}_{14}\text{N})_2[\text{SnCl}_6]$ , and  $(\text{C}_8\text{H}_{12}\text{N})_2[\text{SnCl}_6]$  were used as starting sets. The electronic exchange-correlation energy (XC) is treated using the generalized gradient approximations (GGA) schemes of Perdew and Wang PW91 [60] and of Perdew–Burke–Ernzerhof (PBE) [60,61]. The Van der Waals interactions were taken into account by using the DFT+D method by means of Ortmann, Bechstedt, and Schmidt (OBS) correction to PW91 [62], as well as Tkatchenko and Scheffler (TS) [63] and Grimme [64] corrections to PBE.

The norm-conserving pseudopotential was used to describe the ionic core and valence electron interactions. An energy cutoff of 500 eV was set for the plane wave basis and  $2 \times 2 \times 2$  special Monkhorst–Pack [65,66] k-point mesh for the Brillouin zone (BZ) was adopted for the four structures  $\text{NH}_3(\text{CH}_2)_2\text{C}_6\text{H}_5)_2[\text{SnCl}_6]$ ,  $(\text{C}_6\text{H}_{10}\text{N}_2)[\text{SnCl}_6]$ ,  $(\text{C}_9\text{H}_{14}\text{N})_2[\text{SnCl}_6]$ , and  $(\text{C}_8\text{H}_{12}\text{N})_2[\text{SnCl}_6]$ . To determine the minimum energy of the crystal structure, the Broyden–Fletcher–Goldfarb–Shannon (BFGS) algorithm [67] was used. The convergence criteria of the total energy, atomic force, and maximum displacement were  $10^{-6}$  eV,  $0.05 \text{ eV \AA}^{-1}$ , and  $0.002 \text{ \AA}$ , respectively.

The two approximations (PBE, PW91) were chosen with the correction methods (TS, Grimme, and OBS) based on literature studies [68–73]. They allow to reproduce the experimental unit cell parameters and consider the Van der Waals interaction by using the corrections. Hybrid approximations, such as HSE, take a long time in the optimization of

geometries and require a workstation, so they are incompatible with the computer used in this work.

Generally, the dispersion corrections use three levels, DFT+D1, DFT+D2, and DFT+D3, and it is well known that the DFT+D3 correction with the three varieties (DFT-D3(0), DFT-D3(BJ), DFT-D3(CSO)), which is the recent development of the DFT+D method, gives more coherent results than DFT+D1 and DFT+D2 [74]. The DFT+D3(0) was proposed by Chai and Head-Gordon [75] for a modified DFT-D2 variant and then improved by Grimme and coworkers [64]. The DFT+D3(0) was implemented in Castep code and was used in this work as Grimme correction [76,77]. The TS schemes developed by Tkatchenko and Scheffler [63] and OBS schemes developed by Ortman, Bechstedt, and Schmidt [62] used in this work with the GGA-PBE method correspond to the DFT+D2 [62,63]

It is well known that the use of the spin orbital coupling (SOC) effect in the DFT calculation by using the “fully-relativistic” option enormously improves the results of the electronic structure calculation and the prediction of the optical, thermodynamic, and magnetic properties [78–81], but since the limitation of the computer this option was not used in this study.

It is well-known that the variation in the unit cell parameters may modify the value of the calculated optical gap. Thus, to eliminate this possible confusion, we propose to determine the effect of the Van der Waals interaction on the electronic structure with and without unit cell optimization.

The experimental and optimized structure were compared via the Bilbao crystallographic server [82], which allows to provide the atomic displacement, evaluate the structure similarity (s), similarity function  $\Delta$  (the smaller Delta indicates more similar structures), and maximum and average deviation ( $d_{\max}$  and  $d_{\text{av}}$ ).

#### 4. Conclusions

This work investigated the electronic structure and optical properties of four tin-based 0D hybrid perovskites. The effect of Van der Waals interaction on the crystal and electronic structure was studied using various optimization methods. The dielectric function and partial density of states allowed to determine the nature of the first transition in each compound. The obtained results enabled us to explain the variation in the optical energy gap in the three structures (a), (c), and (d). The structure (b) was not affected by Van der Waals interaction, and the variation in optical energy gap was caused by changes in the unit cell and atom positions. The Bilbao crystallographic server was used to compare the experimental and optimized structures, and the results showed a good match when using the DFT+D methods. The various methods for crystal structure optimization have a minor effect on the absorption curve but preserve the overall profile. This work could be improved by the use of other DFT+D3 methods and by comparing the obtained results with experimental measurements of the optical gap and for the electronic transition. In addition, the use of the SOC effect in the DFT calculation may give more coherent results.

**Author Contributions:** Conceptualization, H.F., Y.B.S. and Y.A.-D.; methodology, H.F., Y.B.S. and Y.A.-D.; software, Y.B.S.; validation, H.F., Y.B.S. and Y.A.-D.; investigation, H.F., Y.B.S. and Y.A.-D.; data curation, H.F. and Y.B.S.; writing—original draft preparation, H.F., Y.B.S. and Y.A.-D.; writing—review and editing, H.F., Y.B.S. and Y.A.-D.; project administration, H.F.; funding acquisition, H.F. All authors have read and agreed to the published version of the manuscript.

**Funding:** This research was funded by the Deputyship for Research and Innovation, Ministry of Education in Saudi Arabia, grant number IFP-IMSIU202201.

**Data Availability Statement:** Not applicable.

**Acknowledgments:** The authors extend their appreciation to the Deputyship for Research and Innovation, Ministry of Education in Saudi Arabia, for funding this research work through project number IFP-IMSIU202201.

**Conflicts of Interest:** The authors declare no conflict of interest.

## References

1. Saidaminov, M.I.; Almutlaq, J.; Sarmah, S.; Dursun, I.; Zhumekenov, A.A.; Begum, R.; Pan, J.; Cho, N.; Mohammed, O.F.; Bakr, O.M. Pure Cs<sub>4</sub>PbBr<sub>6</sub>: Highly luminescent zero-dimensional perovskite solids. *ACS Energy Lett.* **2016**, *1*, 840–845. [[CrossRef](#)]
2. Chen, L.J.; Dai, J.H.; Lin, J.D.; Mo, T.S.; Lin, H.P.; Yeh, H.C.; Chuang, Y.C.; Jiang, S.A.; Lee, C.R. Wavelength-tunable and highly stable perovskite-quantum-dot-doped lasers with liquid crystal lasing cavities. *ACS Appl. Mater. Interfaces* **2018**, *10*, 33307–33315. [[CrossRef](#)] [[PubMed](#)]
3. Xing, G.; Kumar, M.H.; Chong, W.K.; Liu, X.; Cai, Y.; Ding, H.; Asta, M.; Grätzel, M.; Mhaisalkar, S.; Mathews, N. Solution-processed tin-based perovskite for near-infrared lasing. *Adv. Mater.* **2016**, *28*, 8191–8196. [[CrossRef](#)]
4. Yu, W.; Li, F.; Yu, L.; Niazi, M.R.; Zou, Y.; Corzo, D.; Basu, A.; Ma, C.; Dey, S.; Tietze, M.L. Single crystal hybrid perovskite field-effect transistors. *Nat. Commun.* **2018**, *9*, 1–10. [[CrossRef](#)] [[PubMed](#)]
5. Gao, Y.; Wei, Z.; Yoo, P.; Shi, E.; Zeller, M.; Zhu, C.; Liao, P.; Dou, L. Highly stable lead-free perovskite field-effect transistors incorporating linear  $\pi$ -conjugated organic ligands. *J. Am. Chem. Soc.* **2019**, *141*, 15577–15585. [[CrossRef](#)] [[PubMed](#)]
6. Kasel, T.W.; Deng, Z.; Mroz, A.M.; Hendon, C.H.; Butler, K.T.; Canepa, P. Metal-free perovskites for non linear optical materials. *Chem. Sci.* **2019**, *10*, 8187–8194. [[CrossRef](#)]
7. Xu, J.; Li, X.; Xiong, J.; Yuan, C.; Semin, S.; Rasing, T.; Bu, X.H. Nonlinear Optical Perovskites: Halide Perovskites for Nonlinear Optics (Adv. Mater. 3/2020). *Adv. Mater.* **2020**, *32*, 2070017. [[CrossRef](#)]
8. Liu, Q.; Yin, J.; Zhang, B.B.; Chen, J.K.; Zhou, Y.; Zhang, L.M.; Wang, L.M.; Zhao, Q.; Hou, J.; Shu, J. Theory-Guided Synthesis of Highly Luminescent Colloidal Cesium Tin Halide Perovskite Nanocrystals. *J. Am. Chem. Soc.* **2021**, *143*, 5470–5480. [[CrossRef](#)]
9. Ozório, M.S.; Srikanth, M.; Besse, R.; Da Silva, J.L. The role of the A-cations in the polymorphic stability and optoelectronic properties of lead-free ASnI<sub>3</sub> perovskites. *Phys. Chem. Chem. Phys.* **2021**, *23*, 2286–2297. [[CrossRef](#)]
10. Duan, X.; Liu, F.; Kwon, H.; Byun, Y.; Minn, I.; Cai, X.; Zhang, J.; Pomper, M.G.; Yang, Z.; Xi, Z. (S)-3-(Carboxyformamido)-2-(3-(carboxymethyl) ureido) propanoic acid as a novel PSMA targeting scaffold for prostate cancer imaging. *J. Med. Chem.* **2020**, *63*, 3563–3576. [[CrossRef](#)]
11. Zhou, L.; Liao, J.F.; Huang, Z.G.; Wei, J.H.; Wang, X.D.; Chen, H.Y.; Kuang, D.B. Intrinsic self-trapped emission in 0D lead-free (C<sub>4</sub>H<sub>14</sub>N<sub>2</sub>)<sub>2</sub>In<sub>2</sub>Br<sub>10</sub> single crystal. *Angew. Chem.* **2019**, *131*, 15581–15586. [[CrossRef](#)]
12. Pious, J.K.; Katre, A.; Muthu, C.; Chakraborty, S.; Krishna, S.; Vijayakumar, C. Zero-dimensional lead-free hybrid perovskite-like material with a quantum-well structure. *Chem. Mater.* **2019**, *31*, 1941–1945. [[CrossRef](#)]
13. Yavari, M.; Ebadi, F.; Meloni, S.; Wang, Z.S.; Yang, T.C.J.; Sun, S.; Schwartz, H.; Wang, Z.; Niesen, B.; Durantini, J. How far does the defect tolerance of lead-halide perovskites range? The example of Bi impurities introducing efficient recombination centers. *J. Mater. Chem. A* **2019**, *7*, 23838–23853. [[CrossRef](#)]
14. Ke, W.; Kanatzidis, M.G. Prospects for low-toxicity lead-free perovskite solar cells. *Nat. Commun.* **2019**, *10*, 965. [[CrossRef](#)] [[PubMed](#)]
15. Ali, R.; Hou, G.J.; Zhu, Z.G.; Yan, Q.B.; Zheng, Q.R.; Su, G. Predicted lead-free perovskites for solar cells. *Chem. Mater.* **2018**, *30*, 718–728. [[CrossRef](#)]
16. Kamat, P.V.; Bisquert, J.; Buriak, J. Lead-free perovskite solar cells. *ACS Energy Lett.* **2017**, *2*, 904–905. [[CrossRef](#)]
17. Giustino, F.; Snaith, H.J. Toward lead-free perovskite solar cells. *ACS Energy Lett.* **2016**, *1*, 1233–1240. [[CrossRef](#)]
18. Gómez, A.; Wang, Q.; Goñi, A.R.; Campoy-Quiles, M.; Abate, A. Ferroelectricity-free lead halide perovskites. *Energy Environ. Sci.* **2019**, *12*, 2537–2547. [[CrossRef](#)]
19. Ozório, M.S.; Oliveira, W.X.; Silveira, J.F.; Nogueira, A.F.; Da Silva, J.L. Novel zero-dimensional lead-free bismuth-based perovskites: From synthesis to structural and optoelectronic characterization. *Mater. Adv.* **2020**, *1*, 3439–3448. [[CrossRef](#)]
20. Chu, K.B.; Xie, J.L.; Chen, W.J.; Lu, W.X.; Song, J.L.; Zhang, C. A novel bismuth-based hybrid material with highly activity for fast removal of rhodamine B under dark conditions. *Polyhedron* **2018**, *151*, 146–151. [[CrossRef](#)]
21. Zhou, C.; Lin, H.; Tian, Y.; Yuan, Z.; Clark, R.; Chen, B.; van de Burgt, L.J.; Wang, J.C.; Zhou, Y.; Hanson, K. Luminescent zero-dimensional organic metal halide hybrids with near-unity quantum efficiency. *Chem. Sci.* **2018**, *9*, 586–593. [[CrossRef](#)]
22. Pandech, N.; Kongnok, T.; Palakawong, N.; Limpijumngong, S.; Lambrecht, W.R.; Jungthawan, S. Effects of the van der Waals Interactions on Structural and Electronic Properties of CH<sub>3</sub>NH<sub>3</sub>(Pb, Sn)(I, Br, Cl) 3 Halide Perovskites. *ACS Omega* **2020**, *5*, 25723–25732. [[CrossRef](#)] [[PubMed](#)]
23. Ozório, M.S.; Dias, A.C.; Silveira, J.F.; Da Silva, J.L. Theoretical Investigation of the Role of Anion and Trivalent Cation Substitution in the Physical Properties of Lead-Free Zero-Dimensional Perovskites. *J. Phys. Chem. C* **2022**, *126*, 7245–7255. [[CrossRef](#)]
24. Knutson, J.L.; Martin, J.D.; Mitzi, D.B. Tuning the band gap in hybrid tin iodide perovskite semiconductors using structural templating. *Inorg. Chem.* **2005**, *44*, 4699–4705. [[CrossRef](#)] [[PubMed](#)]
25. Saparov, B.; Mitzi, D.B. Organic–inorganic perovskites: Structural versatility for functional materials design. *Chem. Rev.* **2016**, *116*, 4558–4596. [[CrossRef](#)]
26. Moussa, O.B.; Chebbi, H.; Arfaoui, Y.; Falvello, L.R.; Tomas, M.; Zid, M.F. Structural study, vibrational and optical properties, Hirshfeld surface analysis and DFT investigation of a novel organic cation hexachloridostannate (IV), (C<sub>5</sub>H<sub>8</sub>N<sub>3</sub>)<sub>2</sub>[SnCl<sub>6</sub>]. *J. Mol. Struct.* **2019**, *1195*, 344–354. [[CrossRef](#)]
27. Sayer, I.; Dege, N.; Ghalla, H.; Moliterni, A.; Naili, H. Crystal structure, DFT studies and thermal characterization of new luminescent stannate (IV) based inorganic-organic hybrid compound. *J. Mol. Struct.* **2021**, *1224*, 129266. [[CrossRef](#)]

28. Feddaoui, I.; Abdelbaky, M.S.; García-Granda, S.; Essalah, K.; Nasr, C.B.; Mrad, M. Synthesis, crystal structure, vibrational spectroscopy, DFT, optical study and thermal analysis of a new stannate (IV) complex based on 2-ethyl-6-methylanilinium ( $C_9H_{14}N$ )<sub>2</sub> [SnCl<sub>6</sub>]. *J. Mol. Struct.* **2019**, *1186*, 31–38. [[CrossRef](#)]
29. Mathlouthi, M.; Valkonen, A.; Rzaigui, M.; Smirani, W. Structural characterization, spectroscopic, thermal, AC conductivity and dielectric properties and antimicrobial studies of ( $C_8H_{12}N$ )<sub>2</sub> [SnCl<sub>6</sub>]. *Phase Transit.* **2017**, *90*, 399–414. [[CrossRef](#)]
30. Ferjani, H. Crystal structure, optical property and Hirshfeld surface analysis of bis [1-(prop-2-en-1-yl)-1H-imidazol-3-ium] hexachloridostannate (IV). *Acta Crystallogr. Sect. E Crystallogr. Commun.* **2020**, *76*, 1624–1628. [[CrossRef](#)]
31. El-Mellouhi, F.; Marzouk, A.; Bentría, E.T.; Rashkeev, S.N.; Kais, S.; Alharbi, F.H. Hydrogen bonding and stability of hybrid organic–inorganic perovskites. *ChemSusChem* **2016**, *9*, 2648–2655. [[CrossRef](#)]
32. Yu, C.J.; Jong, U.G.; Ri, M.H.; Ri, G.C.; Pae, Y.H. Electronic structure and photoabsorption property of pseudocubic perovskites CH<sub>3</sub>NH<sub>3</sub>PbX<sub>3</sub> (X = I, Br) including van der Waals interaction. *J. Mater. Sci.* **2016**, *51*, 9849–9854. [[CrossRef](#)]
33. Srikant, V.; Clarke, D.R. On the optical band gap of zinc oxide. *J. Appl. Phys.* **1998**, *83*, 5447–5451. [[CrossRef](#)]
34. Zolfaghari, P.; De Wijs, G.; De Groot, R. The electronic structure of organic–inorganic hybrid compounds:(NH<sub>4</sub>)<sub>2</sub>CuCl<sub>4</sub>, (CH<sub>3</sub>NH<sub>3</sub>)<sub>2</sub>CuCl<sub>4</sub> and (C<sub>2</sub>H<sub>5</sub>NH<sub>3</sub>)<sub>2</sub>CuCl<sub>4</sub>. *J. Phys. Condens. Matter* **2013**, *25*, 295502. [[CrossRef](#)] [[PubMed](#)]
35. Liu, X.; Yang, Z.; Ge, C.; Li, H.; Hao, M.; Wan, C.; Song, Y.; Li, B.; Dong, Q. Multiple Hydrogen Bond-Induced Structural Distortion for Broadband White-Light Emission in Two-Dimensional Perovskites. *CCS Chem.* **2021**, *3*, 2576–2583. [[CrossRef](#)]
36. Bernasconi, A.; Page, K.; Dai, Z.; Tan, L.Z.; Rappe, A.M.; Malavasi, L. Ubiquitous Short-Range Distortion Hybrid Perovskites Hydrogen-Bonding role: The MAPbCl<sub>3</sub> case. *J. Phys. Chem. C* **2018**, *122*, 28265–28272. [[CrossRef](#)]
37. Kaiba, A.; Geesi, M.H.; Riadi, Y.; Ibnouf, E.O.; Aljohani, T.A.; Guionneau, P. A new Organic–Inorganic hybrid compound (NH<sub>3</sub>(CH<sub>2</sub>)<sub>2</sub>C<sub>6</sub>H<sub>5</sub>)<sub>2</sub>[SnCl<sub>6</sub>]: Crystal structure, characterization, Hirshfeld surface analysis, DFT calculation, vibrational properties and biological evaluation. *J. Solid State Chem.* **2021**, *304*, 122587. [[CrossRef](#)]
38. Shannon, R.D. Revised effective ionic radii and systematic studies of interatomic distances in halides and chalcogenides. *Acta Crystallogr. Sect. A Cryst. Phys. Diffr. Theor. Gen. Crystallogr.* **1976**, *32*, 751–767. [[CrossRef](#)]
39. Gao, W.; Gao, X.; Abtew, T.A.; Sun, Y.Y.; Zhang, S.; Zhang, P. Quasiparticle band gap of organic-inorganic hybrid perovskites: Crystal structure, spin-orbit coupling, and self-energy effects. *Phys. Rev. B* **2016**, *93*, 085202. [[CrossRef](#)]
40. Laref, A.; Al-Enazi, M.; Al-Qahtani, H.; Laref, S.; Wu, X. Impact of fluorine on organic cation for determining the electronic and optical properties of CH<sup>3-</sup> xF<sub>x</sub>NH<sub>3</sub>PbI<sub>3</sub> (x = 0, 1, 2, 3) hybrid perovskites-based photovoltaic devices. *Sol. Energy* **2019**, *177*, 517–530. [[CrossRef](#)]
41. Gebhardt, J.; Kim, Y.; Rappe, A.M. Influence of the dimensionality and organic cation on crystal and electronic structure of organometallic halide perovskites. *J. Phys. Chem. C* **2017**, *121*, 6569–6574. [[CrossRef](#)]
42. Maheshwari, S.; Patwardhan, S.; Schatz, G.C.; Renaud, N.; Grozema, F.C. The effect of the magnitude and direction of the dipoles of organic cations on the electronic structure of hybrid halide perovskites. *Phys. Chem. Chem. Phys.* **2019**, *21*, 16564–16572. [[CrossRef](#)] [[PubMed](#)]
43. Ferjani, H.; Ben Smida, Y.; Onwudiwe, D.C.; Elamin, N.Y.; Ezzine, S.; Almotlaq, N.S. An Experimental and Theoretical Study of the Optical Properties of (C<sub>2</sub>H<sub>7</sub>N<sub>4</sub>O)<sub>2</sub>BiCl<sub>5</sub> for an Optoelectronic Application. *Inorganics* **2022**, *10*, 48. [[CrossRef](#)]
44. Adala, N.; Marzougui, B.; Smida, Y.B.; Marzouki, R.; Ferhi, M.; Onwudiwe, D.C.; Hamzaoui, A.H. An experimental and theoretical study of the structural, optical, electrical, and dielectric properties of PrAsO<sub>4</sub>. *J. Alloys Compd.* **2022**, *910*, 164894. [[CrossRef](#)]
45. Lakhdar, M.H.; Smida, Y.B.; Amlouk, M. Synthesis, optical characterization and DFT calculations of electronic structure of Sb<sub>2</sub>O<sub>3</sub> films obtained by thermal oxidation of Sb<sub>2</sub>S<sub>3</sub>. *J. Alloys Compd.* **2016**, *681*, 197–204. [[CrossRef](#)]
46. Lee, I.H.; Martin, R.M. Applications of the generalized-gradient approximation to atoms, clusters, and solids. *Phys. Rev. B* **1997**, *56*, 7197. [[CrossRef](#)]
47. Juran, T.R.; Smeu, M. Hybrid density functional theory modeling of Ca, Zn, and Al ion batteries using the Chevrel phase Mo<sub>6</sub>S<sub>8</sub> cathode. *Phys. Chem. Chem. Phys.* **2017**, *19*, 20684–20690. [[CrossRef](#)]
48. Umari, P.; Mosconi, E.; Angelis, F.D. Relativistic GW calculations on CH<sub>3</sub>NH<sub>3</sub>PbI<sub>3</sub> and CH<sub>3</sub>NH<sub>3</sub>SnI<sub>3</sub> Perovskites for Solar Cell Applications. *Sci. Rep.* **2014**, *4*, 4467. [[CrossRef](#)]
49. Chang, L.; Besteiro, L.V.; Sun, J.; Santiago, E.Y.; Gray, S.K.; Wang, Z.; Govorov, A.O. Electronic structure of the plasmons in metal nanocrystals: Fundamental limitations for the energy efficiency of hot electron generation. *ACS Energy Lett.* **2019**, *4*, 2552–2568. [[CrossRef](#)]
50. Toll, J.S. Causality and the dispersion relation: Logical foundations. *Phys. Rev.* **1956**, *104*, 1760. [[CrossRef](#)]
51. Gajdoš, M.; Hummer, K.; Kresse, G.; Furthmüller, J.; Bechstedt, F. Linear optical properties in the projector-augmented wave methodology. *Phys. Rev. B* **2006**, *73*, 045112. [[CrossRef](#)]
52. Peter, Y.Y.; Cardona, M. *Electronic Band Structures, Fundamentals of Semiconductors*; Springer: Berlin/Heidelberg, Germany, 1996; pp. 17–105.
53. Cardona, M.; Peter, Y.Y. *Fundamentals of Semiconductors*; Springer: Berlin/Heidelberg, Germany, 2005.
54. Smida, Y.B.; Ferjani, H.; Boukhachem, A.; Onwudiwe, D.C.; Elamin, N.Y.; Hamzaoui, A.H. Ab initio study of the optoelectronic properties of α-Ba<sub>2</sub>SnS<sub>4</sub>. *Mater. Sci. Semicond. Process.* **2022**, *150*, 106917. [[CrossRef](#)]
55. Flor, G.; Orobengoa, D.; Tasci, E.; Perez-Mato, J.M.; Aroyo, M.I. Comparison of structures applying the tools available at the Bilbao Crystallographic Server. *J. Appl. Crystallogr.* **2016**, *49*, 653–664. [[CrossRef](#)]

56. Papi, H.; Jalali-Asadabadi, S.; Nourmohammadi, A.; Ahmad, I.; Nematollahia, J.; Yazdanmehr, M. Optical properties of ideal  $\gamma$ -Al<sub>2</sub>O<sub>3</sub> and with oxygen point defects: An ab initio study. *RSC Adv.* **2015**, *5*, 55088–55099. [[CrossRef](#)]
57. Bergerhoff, G.; Berndt, M.; Brandenburg, K.; Degen, T. Concerning inorganic crystal structure types. *Acta Crystallogr. Sect. B Struct. Sci.* **1999**, *55*, 147–156. [[CrossRef](#)] [[PubMed](#)]
58. Segall, M.; Lindan, P.J.; Probert, M.A.; Pickard, C.J.; Hasnip, P.J.; Clark, S.; Payne, M. First-principles simulation: Ideas, illustrations and the CASTEP code. *J. Phys. Condens. Matter* **2002**, *14*, 2717. [[CrossRef](#)]
59. Clark, S.J.; Segall, M.D.; Pickard, C.J.; Hasnip, P.J.; Probert, M.I.; Refson, K.; Payne, M.C. First principles methods using CASTEP. *Z. Krist.-Cryst. Mater.* **2005**, *220*, 567–570. [[CrossRef](#)]
60. Perdew, J.P.; Burke, K.; Ernzerhof, M. Generalized gradient approximation made simple. *Phys. Rev. Lett.* **1996**, *77*, 3865. [[CrossRef](#)] [[PubMed](#)]
61. Ernzerhof, M.; Scuseria, G.E. Assessment of the Perdew–Burke–Ernzerhof exchange–correlation functional. *J. Chem. Phys.* **1999**, *110*, 5029–5036. [[CrossRef](#)]
62. Ortman, F.; Bechstedt, F.; Schmidt, W. Semiempirical van der Waals correction to the density functional description of solids and molecular structures. *Phys. Rev. B* **2006**, *73*, 205101. [[CrossRef](#)]
63. Tkatchenko, A.; Scheffler, M. Accurate molecular van der Waals interactions from ground-state electron density and free-atom reference data. *Phys. Rev. Lett.* **2009**, *102*, 073005. [[CrossRef](#)] [[PubMed](#)]
64. Grimme, S. Density functional theory with London dispersion corrections. *Wiley Interdiscip. Rev. Comput. Mol. Sci.* **2011**, *1*, 211–228. [[CrossRef](#)]
65. Monkhorst, H.J.; Pack, J.D. Special points for Brillouin-zone integrations. *Phys. Rev. B* **1976**, *13*, 5188. [[CrossRef](#)]
66. Pack, J.D.; Monkhorst, H.J. “Special points for Brillouin-zone integrations”—A reply. *Phys. Rev. B* **1977**, *16*, 1748. [[CrossRef](#)]
67. Head, J.D.; Zerner, M.C. A Broyden–Fletcher–Goldfarb–Shanno optimization procedure for molecular geometries. *Chem. Phys. Lett.* **1985**, *122*, 264–270. [[CrossRef](#)]
68. Benghia, A.; Dahame, T.; Bentría, B. First principle calculation of physical properties of barium based chalcogenides BaM<sub>4</sub>S<sub>7</sub> (M = Ga, Al); a DFT, DFT-D and hybrid functional HSE06 study. *Opt. Mater.* **2016**, *54*, 269–275. [[CrossRef](#)]
69. Wang, W.; Fan, L.; Wang, G.; Li, Y. CO<sub>2</sub> and SO<sub>2</sub> sorption on the alkali metals doped CaO (100) surface: A DFT-D study. *Appl. Surf. Sci.* **2017**, *425*, 972–977. [[CrossRef](#)]
70. Wu, Q.; Zhu, W.; Xiao, H. Comparative DFT-and DFT-D-based molecular dynamics studies of pressure effects in crystalline 1, 3, 5-triamino-2, 4, 6-trinitrobenzene at room temperature. *RSC Adv.* **2014**, *4*, 53149–53156. [[CrossRef](#)]
71. Liu, Y.; Wang, G.; Gong, X. 2, 4-Diazido-5-iodo-pyrimidine crystal under high pressure: A comparison of DFT and DFT-D studies. *Comput. Theor. Chem.* **2012**, *1000*, 60–69. [[CrossRef](#)]
72. Gao, H.; Wei, W.; Li, L.; Tan, Y.; Tang, Y. Mechanical properties of a 2D lead-halide perovskite, (C<sub>6</sub>H<sub>5</sub>CH<sub>2</sub>NH<sub>3</sub>)<sub>2</sub>PbCl<sub>4</sub>, by nanoindentation and first-principles calculations. *J. Phys. Chem. C* **2020**, *124*, 19204–19211. [[CrossRef](#)]
73. Xu, Z.W.; Zhang, C.R.; Wu, Y.Z.; Gong, J.J.; Wang, W.; Liu, Z.J.; Chen, H.S. Density functional theory study on the electronic structures and related properties of Ag-doped CH<sub>3</sub>NH<sub>3</sub>PbI<sub>3</sub> perovskite. *Results Phys.* **2019**, *15*, 102709. [[CrossRef](#)]
74. Goerigk, L. A comprehensive overview of the DFT-D3 London-dispersion correction. In *Non-Covalent Interactions in Quantum Chemistry and Physics*; Elsevier: Amsterdam, The Netherlands, 2017; pp. 195–219.
75. Chai, J.-D.; Head-Gordon, M. Long-range corrected hybrid density functionals with damped atom–atom dispersion corrections. *Phys. Chem. Chem. Phys.* **2008**, *10*, 6615–6620. [[CrossRef](#)] [[PubMed](#)]
76. Grimme, S.; Hansen, A.; Brandenburg, J.G.; Bannwarth, C. Dispersion-corrected mean-field electronic structure methods. *Chem. Rev.* **2016**, *116*, 5105–5154. [[CrossRef](#)]
77. Grimme, S.; Antony, J.; Ehrlich, S.; Krieg, H. A consistent and accurate ab initio parametrization of density functional dispersion correction (DFT-D) for the 94 elements. *J. Chem. Phys.* **2010**, *132*, 154104. [[CrossRef](#)]
78. Rao, E.N.; Vaitheeswaran, G.; Reshak, A.H.; Auluck, S. Role of spin–orbit interaction on the nonlinear optical response of CsPbCO<sub>3</sub>F using DFT. *Phys. Chem. Chem. Phys.* **2017**, *19*, 31255–31266.
79. Kormányos, A.; Zólyomi, V.; Drummond, N.D.; Rakyta, P.; Burkard, G.; Fal’ko, V.I. Monolayer MoS<sub>2</sub>: Trigonal warping, the  $\Gamma$  valley, and spin-orbit coupling effects. *Phys. Rev. B* **2013**, *88*, 045416. [[CrossRef](#)]
80. Kormányos, A.; Zólyomi, V.; Drummond, N.D.; Burkard, G. Spin-orbit coupling, quantum dots, and qubits in monolayer transition metal dichalcogenides. *Phys. Rev. X* **2014**, *4*, 011034. [[CrossRef](#)]
81. Pan, J.; Metzger, W.K.; Lany, S. Spin-orbit coupling effects on predicting defect properties with hybrid functionals: A case study in CdTe. *Phys. Rev. B* **2018**, *98*, 054108. [[CrossRef](#)]
82. Aroyo, M.I.; Perez-Mato, J.M.; Capillas, C.; Kroumova, E.; Ivantchev, S.; Madariaga, G.; Kirov, A.; Wondratschek, H. Bilbao Crystallographic Server: I. Databases and crystallographic computing programs. *Z. Krist.-Cryst. Mater.* **2006**, *221*, 15–27. [[CrossRef](#)]